

Auto-PICNN: Automated machine learning for physics-informed convolutional neural networks

Wanyun Zhou^a, Xiaowen Chu^{a,*}

^aThe Hong Kong University of Science and Technology (Guangzhou), Guangzhou, 511453, P.R.China

Abstract

Recent advances in deep learning for solving partial differential equations (PDEs) have introduced physics-informed neural networks (PINNs), which integrate machine learning with physical laws. Physics-informed convolutional neural networks (PICNNs) extend PINNs by leveraging CNNs for enhanced generalization and efficiency. However, current PICNNs depend on manual design, and inappropriate designs may not effectively solve PDEs. Furthermore, due to the diversity of physical problems, the ideal network architectures and loss functions vary across different PDEs. It is impractical to find the optimal PICNN architecture and loss function for each specific physical problem through extensive manual experimentation. To surmount these challenges, this paper uses automated machine learning (AutoML) to automatically and efficiently search for the loss functions and network architectures of PICNNs. We introduce novel search spaces for loss functions and network architectures and propose a two-stage search strategy. The first stage focuses on searching for factors and residual adjustment operations that influence the loss function, while the second stage aims to find the best CNN architecture. Experimental results show that our automatic searching method significantly outperforms the manually-designed model on multiple datasets.

Keywords: Deep learning, Partial differential equations, Physics-informed convolutional neural networks, Automatic machine learning

1. Introduction

The traditional numerical methods for solving PDEs mainly rely on finite difference methods and finite element methods [1]. Both methods solve equations by discretizing

*Corresponding author. Email address: xwchu@ust.hk

the domain. Although numerical methods for solving differential equations can yield high-precision solutions, they necessitate very precise discretization, leading to slower solving speed [2]. While utilizing coarse grids for solving is faster, it results in lower accuracy. Moreover, nearly all numerical methods require solutions to be obtained on the predefined grids, making it impossible to freely obtain continuous values between grids [3]. To circumvent this trade-off, the development of deep learning has resulted in using deep neural networks to solve PDEs [4, 5, 6, 7, 8, 9]. Among these approaches, PINNs have become widely adopted [5]. The fundamental concept behind PINNs is to exploit the expressive capabilities of deep neural networks to approximate the solution of a PDE. By incorporating the governing equations as constraints into the loss function, PINNs enable the neural networks to adhere to the physical laws during training. Moreover, PINNs offer advantages in handling high-dimensional and irregular domains encountered in PDE solving [2, 10]. Additionally, training traditional deep learning tasks typically requires a large amount of labeled data. However, obtaining such data can be challenging for certain physical problems. By incorporating physical constraints, PINNs guide the model’s learning process and alleviate the need for extensive labeled data [11].

Existing PINN frameworks are mostly based on Multi-Layer Perceptrons (MLPs). In recent years, PICNNs based on CNNs have begun to emerge [12, 13, 14, 15, 16, 17, 18]. Compared with MLP-based PINNs that require retraining when there is a minor change to the equation, PICNNs can treat physical parameters in PDEs as model inputs, allowing for inference of unknown boundary conditions or source fields without retraining. This characteristic significantly enhances the generalization capabilities of PINNs [13, 14]. Additionally, due to parameter sharing in CNNs, PICNNs may handle large-scale problems more effectively than MLPs [13]. Although PICNNs have been extensively applied in materials science, fluid mechanics, thermodynamics, geology, and other fields [12, 13, 14, 15, 19, 20], there are still some issues: **(1)**: Existing PICNNs are manually designed, and many PDEs may not be solved correctly due to inappropriate network architectures [21, 22]. **(2)**: Different physical problems necessitate solving various types of PDEs, and different types of PDEs may be favored by different neural networks. The search space for the possible architectures of neural networks is huge, and therefore finding the best PICNN architecture through a large number of manual experiments is unrealistic [23]. **(3)**: For different PDE datasets, the computational factors of the loss functions including boundary constraints and convolution kernels in PICNNs are distinct. Moreover, current PICNNs mainly use vanilla loss functions, neglecting the use of weighting strategies for different training points, a technique frequently used in PINNs [1, 24, 25]. However, even within the realm of PINNs, the weighting strategies employed are highly varied across different

PDE datasets. Weighting strategies that are effective on a certain PDE dataset may lead to a significant increase in prediction error on other PDE datasets compared to the vanilla loss function.

To solve the first two issues, currently, only a few studies apply automatic machine learning (AutoML) to automatically design PINN models [21, 23, 26]. However, these studies all focus on MLP-based PINNs, and there is no research investigating the application of AutoML in PICNNs with CNN as the underlying framework. Furthermore, the automatic computation of appropriate loss functions in both PINNs and PICNNs remains unexplored. Therefore, we aim to use AutoML to search for the optimal network architecture and loss function that can effectively reduce prediction errors and improve the accuracy of PICNNs in approximating the solutions of PDEs. To achieve this, we follow a systematic approach outlined as follows: Firstly, we delve into the correlation between the PDE-driven loss and prediction errors within the PICNNs and determine that the prediction error of the validation set will serve as the search objective. Secondly, by considering factors that may influence the accuracy of the loss function, we construct a novel operator-infused loss function search space that encompasses factors as well as a few residual adjustment operations, and then we utilize hyperparameter optimization to explore an appropriate loss function for each dataset. Concurrently, we define the fundamental architecture of PICNNs across different datasets and establish an appropriate search space accordingly. This involves choosing the entire-structured search space instead of the cell-based search space as the overall structure and configurations that constitute the network architecture of PICNNs. Finally, to search for the best network architecture within the search space, we explore two neural architecture search (NAS) methods: multi-trial strategies and one-shot strategies. By leveraging the power of our AutoML approaches, we enhance the accuracy of PICNNs in solving PDEs, surpassing the manually designed state-of-the-art models significantly. The contributions of this paper can be summarized as follows:

- We are the first to apply AutoML in PICNNs, addressing the challenge that manually finding the optimal PICNN architecture and loss function for each specific PDE dataset is impractical.
- A novel operator-infused loss function search space is proposed. This search space not only considers the factors affecting the computation of loss functions in PICNNs but also combines some existing commonly used weighting strategies in PINNs into PICNNs.
- We design appropriate search spaces for the network architectures of PICNNs, which ensure a more effective and holistic search.

- Our two-stage search strategy exhibits significant improvements over the existing manually-designed PICNNs on all five datasets.

2. Background

2.1. Physics-Informed convolutional neural networks (PICNNs)

Consider a parametric PDE in the spatial domain:

$$\begin{aligned}\mathcal{F}[u(\mathbf{x}), \mu] &= f(\mathbf{x}), \quad \mathbf{x} \in \Omega \\ \mathcal{B}[u(\mathbf{x}), \mu] &= g(\mathbf{x}), \quad \mathbf{x} \in \partial\Omega\end{aligned}\tag{1}$$

where $u(\mathbf{x})$ denotes the solution of the parametric PDE, \mathcal{F} is the differential operator of the PDE, \mathcal{B} is the boundary condition operator, Ω is the domain of the equation, and $\partial\Omega$ is the boundary of the domain. The parameter μ can represent either the parameters or the source fields of the PDE, and the spatial dimension of \mathbf{x} is 2. In PICNNs, the input of the CNN is usually the parameter field $\mu(\mathbf{x})$. After passing through the CNN, the output represents the values of the solution of the PDE at each training point.

The construction of the loss function is as follows:

$$L(\theta) = \lambda_r L_r(\theta) + \lambda_b L_b(\theta)\tag{2}$$

$$L_r(\theta) = \frac{1}{N_r} \sum_{n=1}^{N_r} |\mathcal{F}[u_\theta(x_r^n)] - f(x_r^n)|^2\tag{3}$$

$$L_b(\theta) = \frac{1}{N_b} \sum_{n=1}^{N_b} |\mathcal{B}[u_\theta(x_b^n)] - g(x_b^n)|^2\tag{4}$$

where $\{x_r^n\}_{n=1}^{N_r}$ are the residual points sampled within the domain, $\{x_b^n\}_{n=1}^{N_b}$ are the boundary points, and λ_r, λ_b are coefficients of the PDE residual term L_r , boundary condition loss term L_b . $u_\theta(x)$ represents the CNN used to approximate the solution of the PDEs where θ are the trainable parameters of the neural network. The basic architecture of the CNNs has many options, such as standard CNN structure, UNet [14, 27], DenseNet [12, 28], and SegNet [29]. In this paper, a simple CNN consisting of stacked convolutional layers and ReLU activation functions is used for PDEs with different boundary conditions or different boundary geometries. For PDEs with different source fields, UNet is used as the framework. The process of computing the partial derivatives of the PDEs in PICNNs can be approximated by numerical methods.

2.2. Related work

2.2.1. Physics-informed convolutional networks (PICNNs)

PICNNs are a type of physics-informed neural network based on the framework of CNNs. Recently, an increasing number of research articles have been utilizing them to handle parameter-dependent or varying source fields PDEs. Zhu et al. proposed a CNN-based encoder-decoder structure [12] to construct a surrogate model for Darcy flow and perform uncertainty quantification analysis without labeled data [12] while Zhang et al. developed a PICNN for simulating transient two-phase Darcy flows in heterogeneous reservoir models with source/sink terms [19]. Both Ren et al. and Mavi et al. integrate LSTM into PICNN to solve spatiotemporal PDEs [30, 17]. Gao et al. introduced coordinate transformations to enable the application of PICNNs on irregular domains [13]. Zhao et al. presented a UNet-based PICNN for predicting temperature fields with different heat source layouts [14]. Zhang et al. proposed a method based on multi-receptive field PICNNs [15] to solve PDEs with varying grid resolutions and use Taylor polynomials with high-order finite differences to fill in virtual nodes near the boundary.

2.2.2. AutoML in PINNs

Though AutoML has not been used to solve PICNNs, a few studies apply it to automatically design PINN models. Guo et al. were the first to use existing hyperparameter optimization methods in AutoML to determine the number of layers and neurons per layer for PINNs in groundwater flow problems [26]. Wang et al. decoupled some hyperparameters through pre-experiments and proposed a systematic, automated PINN hyperparameter optimization method [23]. Wu et al. utilized a reinforcement learning strategy to find high-accuracy PINNs for predicting the internal parameters of power electronic converters under different hardware constraints [21]. Wang et al. combined the gradient optimization methods with MLP and designed a NAS-guided physics-informed neural network to solve PDEs [31]. Xie et al. pointed out that the trial functions need to be designed separately for different boundary conditions in PINNs so a boundary fitting framework was designed to automatically search for the boundary dependent trial function [32].

However, all these methods are designed for searching hyperparameters within MLPs, not CNNs. Their MLP structure also means that all these methods are tailored for non-parametric PDEs (the definition can be seen in section 3.1), which requires retraining when certain parameters within the equations are changed. Moreover, when performing AutoML for non-parametric PDEs, the search objective can only select a PDE-driven loss, which is shown to be inappropriate in section 3.1. Notably, even though Wang et al.[31] and Guo et al.[26] sampled a subset of training points

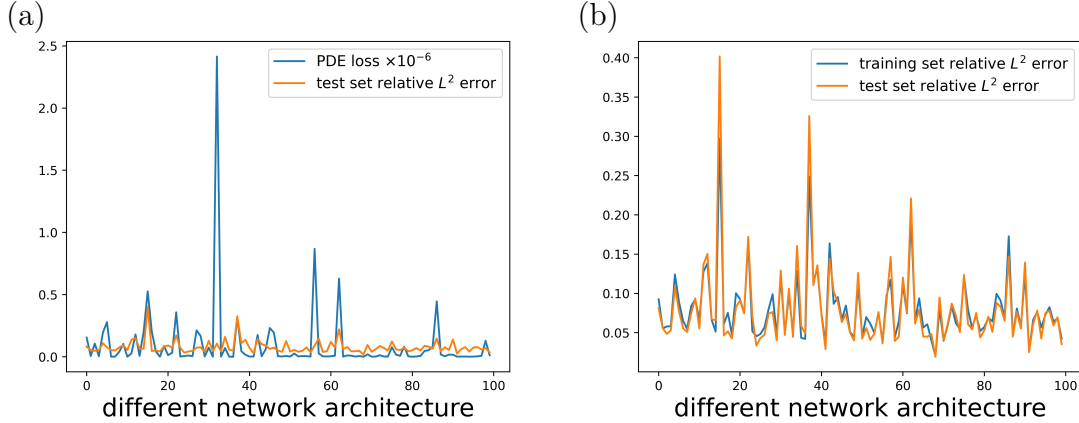


Figure 1: PDE-driven loss and prediction error for different network architectures. (a) shows the PDE-driven loss of the training set and prediction error of the test set across different network architectures. (b) shows the prediction error of the training set and the test set across different network architectures

and used their relative L^2 error as the search objective, both methods cause test set data leakage because of the non-parametric setting. Therefore, due to the differences in search space and search objectives, these methods cannot be directly applied to PICNNs.

3. Method

3.1. Search objective

PDEs can be divided into non-parametric and parametric PDEs. Non-parametric PDEs are defined solely by the variables and their derivatives, without external parameters. Parametric PDEs are defined not only in terms of independent variables but also include varying physical parameters such as source fields and geometric factors, that can influence the solution. Since each parameter corresponds to a specific PDE, varying physical parameters allow the dataset of parametric PDEs to contain multiple samples. Meanwhile, non-parametric PDEs, lacking varying parameters, are limited to a single sample. Therefore, when dealing with non-parametric PDEs, we can only choose the PDE-driven loss as the search objective to determine the loss function and architecture which is what Wang et al. did in their paper [23]. However, for PICNNs, the PDE-driven loss and relative prediction error are not uniform across different architectures. Taking the parametric heat equation as an example, Figure 1 (a) shows that when the PDE-driven loss is high, the relative L^2 error can be low,

and vice versa. The discrepancy observed may be attributed to the phenomenon that using some neural network architectures to solve PDEs may fall into the trivial solutions. In these cases, the training of PICNNs minimizes PDE-driven loss by adopting simplistic solutions that, while adhering to some basic PDE constraints, fail to capture the full complexity of the physical problem, leading to higher relative L^2 errors. Such outcomes highlight the fact that the PDE-driven loss alone may not provide a reliable indication of the actual prediction performance, which suggests that it is difficult for non-parametric PDEs to find an appropriate search objective. In contrast, for parametric PDEs, we can split the dataset into the training and the test set, as shown in Figure 1 (b), the prediction error of the training set and the test set is relatively uniform.

Therefore, it is beneficial to choose parametric PDEs as datasets due to the more consistent prediction error behavior observed across the training and test sets. In addition, when the training set is small, it can be treated as a validation set, with its prediction error being the search objective. However, when the training set is large, we only need to select a small number of samples from the training set, generate reference solutions, and use them as the validation set. Taking the prediction error of the validation set as the search objective ensures the effectiveness of the search while maintaining the advantage of PICNNs in saving time and resources without generating labels on a large number of data points.

3.2. Loss function construction

In PICNNs, the vanilla MSE loss function (see Equation 2) is commonly used but the construction of the proper loss function may vary for different PDEs. To reduce prediction error, it is necessary to find a suitable loss function for a specific PDE dataset. The construction of the loss function may be influenced by the following four factors: the type of constraints on the boundary condition, the calculation of spatial derivatives, the symbolic regression forms of the loss function, and the weighting strategies for different training points.

3.2.1. Soft/Hard constraints

There are two types of constraints on the boundary condition used in PINNs and PICNNs [4]. One is the soft constraint which considers the difference between the boundary condition of network outputs and the real one as a penalty term added to the loss function. The other is the hard constraint that modifies the network outputs such that the boundary conditions can be strictly imposed into the network architecture during training. For the Dirichlet boundary, the known constants on the boundary can be filled by padding operation. For the Neumann boundary, the filled

values can be determined by solving the finite difference from Neumann boundary conditions. Furthermore, our search space, as detailed in Section 3.5, encompasses a novel approach that combines both soft and hard constraints. It has the penalty term of the boundary condition added to the loss function while ensuring that the hard constraints are strictly imposed before the differentiation operations of the PDEs.

3.2.2. Calculation of spatial derivatives

For PDEs in the spatial domain, Sobel filters (used for edge detection in image processing), and finite difference methods can be used to calculate spatial derivatives of different orders [12]. The core idea is to use predefined, untrainable kernels to convolve the input matrix. This convolution process enables the computation of horizontal and vertical gradients of the PDEs at each spatial position. In this paper, four kernels (3x3 Sobel filter, 5x5 Sobel filter, 2nd order accuracy central difference, 4th order accuracy central difference) are employed to calculate spatial differentiation with different orders. The detailed description of the four convolution kernels can be found in Supplementary material A.

3.2.3. Regression loss function

The L^2 physics-informed loss known as the mean square error (MSE) is widely used in both PINNs and PICNNs. However, [33] pointed out that L^2 physics-informed loss may not be a suitable choice for some PDEs. Instead, they chose L^∞ as the form of the regression loss function. Apart from this, the L^1 physics-informed loss known as the mean absolute error (MAE) has also been used [14] in training. Therefore, our search space also takes this factor into consideration.

3.2.4. Weighting strategies for different training points

More and more studies have made advancements in enhancing the components and weights balancing within the vanilla loss function of PINNs based on previous work [5]. Common methods include Residual-based Adaptive Refinement (RAR) [1], Gradient-enhanced PINN (GPINN) [24], self-adaptive loss function [25], and Pixel-level Online Hard Example Mining (P-OHEM) [14]. However, these methods are mainly used in PINNs. We adopt the main idea of these methods and design several operators in the search space such that these methods can be comprised in our search space. Detailed illustrations of these methods are as follows:

1. Inspired by the idea of the Residual-based adaptive refinement (RAR) [1] used in PINNs, we propose the RAR on PICNNs:
 - (i) Train the neural network on the training set for a certain number of epochs.

- (ii) Calculate the residual of the PDE at each training point for each sample in the domain.
 - (iii) For each sample, add the point with the top- N largest residual to its training points.
 - (iv) Repeat steps (i)-(iii) until the specified number of rounds is reached.
2. The core idea of GPINN[24] based on PICNNs is that when the PDE residual is zero, its gradient is also zero, i.e., $\nabla f(x) = \left(\frac{\partial f}{\partial x_1}, \frac{\partial f}{\partial x_2}, \dots, \frac{\partial f}{\partial x_d}\right) = 0, x \in \Omega$ where $f(x)$ is the residual of the PDE. Based on this, the gradient term $\nabla f(x)$ can be added to the vanilla loss function, resulting in the following loss function:

$$L = \lambda_r L_r + \lambda_b L_b + \sum_{i=1}^d \lambda_{g_i} L_{g_i} \quad (5)$$

$$L_{g_i} = \frac{1}{N_g} \sum_{n=1}^{N_g} \text{Unary_op}\left(\frac{\partial f}{\partial x_{g_i}^n}\right), i = 1, 2 \quad (6)$$

where $\{x_{g_i}^n\}_{n=1}^{N_g}$ is the set of residual points and Unary_op is the unary operator (see Section 3.2.5).

3. The core idea of P-OHEM[14] based on PICNNs is to increase the weight of hard examples (training samples with larger PDE loss). Assuming that the error of each pixel in the network output is represented as $r_{i,j}$, the weight of the pixel at position (i, j) can be represented as:

$$w_{i,j} = \eta_1 \frac{r_{i,j} - \min(r)}{\max(r) - \min(e)} \quad (7)$$

where η_1 is a scaling factor.

4. Inspired by the idea of the self-adaptive PINNs [25], we propose the self-adaptive methods on PICNNs. The core idea is to use gradient descent to update the neural network weights w while using gradient ascent to update the self-adaptation weights on each training point. The equations can be written as:

$$w^{k+1} = w^k - \eta_k \nabla_w L(w^k, \lambda_r^k) \quad (8)$$

$$\lambda_r^{k+1} = \lambda_r^k + \rho_r^k \nabla_{\lambda_r} L(w^k, \lambda_r^k) \quad (9)$$

where ρ and η are the learning rate and λ_r is the self-adaptation weights for the residue points.

3.2.5. Operator-infused loss function search space

Figure 2 showed the overall construction of our operator-infused loss function search space for PICNNs. This framework innovatively combines a variety of components of loss functions and comprehensive operators representing different weighting strategies for the computation of loss functions of PICNNs. The candidates for each component in this search space are:

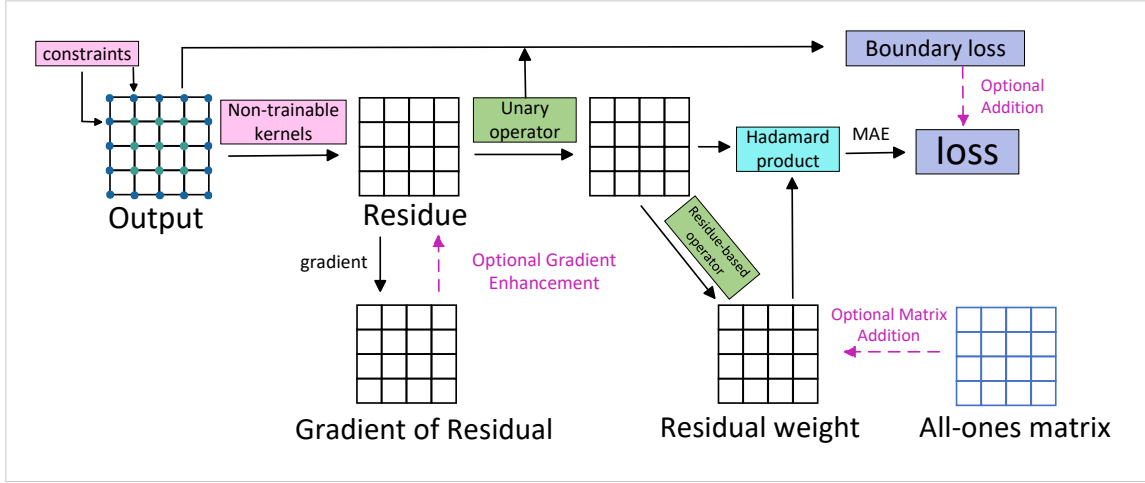


Figure 2: The operator-infused loss function search space

1. **Constraint:** Before performing convolutional differentiation on the model output, the constraint component in the search space determines whether there will be a hard constraint imposed on the output.
2. **Non-Trainable kernels:** We utilize a range of non-trainable convolution kernels as candidates to execute spatial differentiations of various orders to get the residue matrix.
3. **Unary operators on residue:** The residue matrix is transformed by unary operators, including absolute, square, and identity functions.
4. **Optional gradient enhancement of residue:** It determines whether there will be an optional addition that involves enhancing the residue by its gradient.
5. **Residue-based operators for weighting:** These operators manipulate the residue matrix to derive weights for training points. Operations include:
 - (i) **Top- N thresholding:** An operation that sets the highest N elements in the residue matrix to the value 1, while all other elements are set to 0.

- (ii) Normalization: Min-max normalization is used. It transforms each element $r_{i,j}$ in the residue matrix by rescaling it to a value between 0 and 1 based on the minimum and maximum values within the matrix. The formula for min-max normalization is given by Equation 7
- (iii) Pointwise loss gradient: An operation that calculates the derivative of the loss function with respect to the current weight of each training point in the neural network and each point starts with an initial weight of 1.
- (iv) Unitization: An operation that transforms all elements of the residue matrix to the value 1.

For both top- N thresholding and pointwise loss gradient calculation, the weight matrix obtained through residue-based operators will undergo cumulative aggregation across each batch. In contrast, for unitization and normalization, the weight matrix obtained through residue-based operators will be directly utilized as the final weight matrix without cumulative aggregation.

6. **Optional matrix addition:** The weight matrix may be optionally augmented with an all-ones matrix.
7. **Loss boundary addition:** The integration of boundary loss into the final loss computation is an optional choice.

This operator-infused loss function search space not only includes existing strategies mentioned above (see Supplementary material B) but also explores innovative strategies in loss function formulation.

3.3. Search space

The input-output relationship of the networks solving parameterized PDEs is analogous to an image segmentation task. Therefore, for models solving PDEs with varying source fields, we choose the classic image segmentation model UNet[27]. We consider two categories of the search space of UNet: entire-structured search space and cell-based search space.

However, for parameterized PDEs without varying sources, the dataset is generally small. Specifically, for the heat equation with varying boundary conditions, there are only two training samples, and for the Navier-Stokes equation with varying geometries, there are only three training samples. Given the small size of the dataset, the classic models that are widely used in computer vision tasks for segmentation such as UNet[27], FCN[34], DeepLab[35] tend to have a much slower convergence speed and are more prone to overfitting. Therefore the architecture of the search

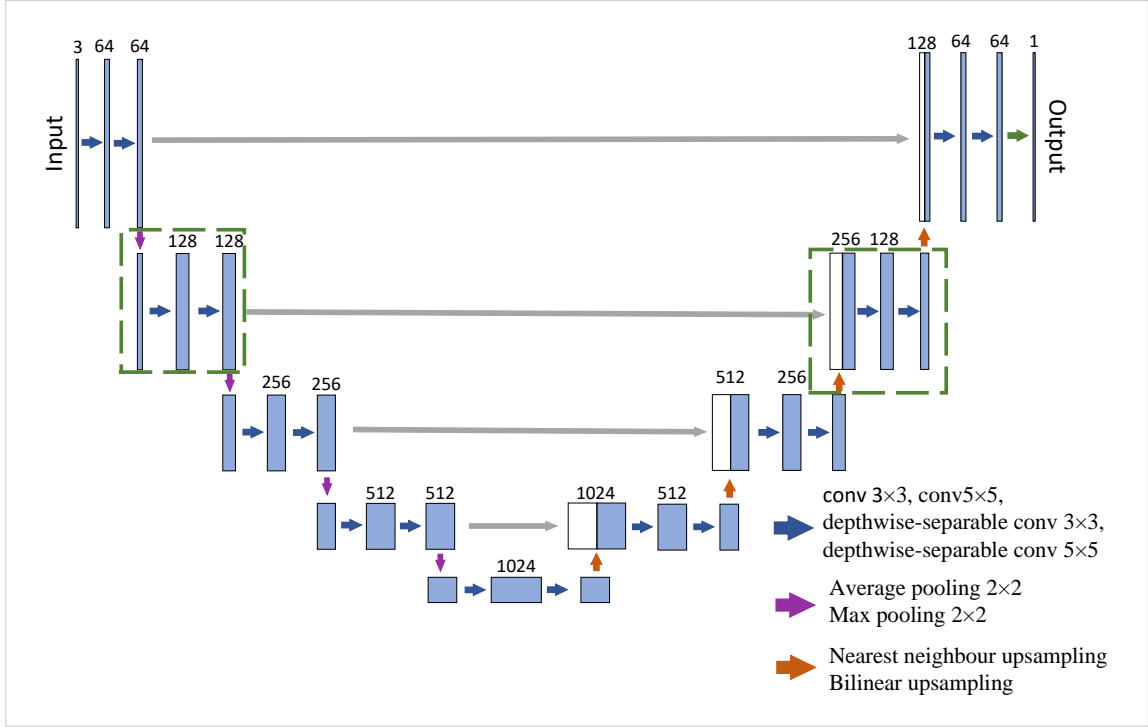


Figure 3: Entire-structured search space based on UNet

space of parameterized PDEs without varying sources is set to a standard but simple CNN composed of stacked convolutional layers and ReLU activation functions. To construct the search space, we choose 3×3 , 5×5 , and 7×7 convolution kernels and their corresponding depth-wise separable convolution kernels as candidates in each layer. Max pooling and average pooling with pooling size being 3 and stride being 1 are also added to the convolutional layers in the middle as candidate operations.

3.3.1. Entire-structured search space

In the entire-structured search space [36], in order to find a network architecture with the best performance, we need to search the entire neural network architecture which includes the operations at each layer (such as convolution, and pooling). Figure 3 shows the search space based on the entire structure of UNet.

For the upsampling operation, references [12, 14] pointed out that using transposed convolution for upsampling would lead to worse prediction results. Based on this, this paper defines the following candidate operations for the convolutional layers, upsampling, and downsampling operations of UNet:

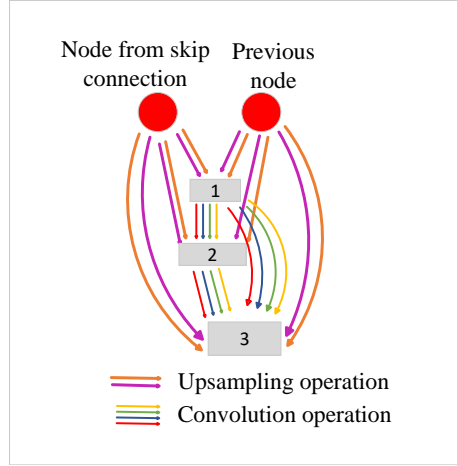


Figure 4: Search space of the upsampling cell

1. operations for downsampling: Max pooling, average pooling.
2. operations for convolutional layer: Standard convolutions with kernel size of 3x3 and 5x5, depth-wise separable convolutions with kernel size of 3x3 and 5x5.
3. operations for upsampling: Bilinear interpolation, Nearest-neighbor interpolation.

Besides, Group Normalization and GeLU activation functions are used as normalization and activation functions.

3.3.2. Cell-based search space

By breaking down the network architecture into repeatable, combinable basic cells, the objective of the cell-based search space is to identify an effective cell structure that can be utilized to construct the full neural network. NAS-UNet [37] was the first to construct a cell-based search space for UNet and perform NAS. As shown in the green box in Figure 3, this paper considers the upsampling/downsampling and two convolutional layers of UNet as a single cell. The construction of the cell combines the search spaces of Darts [38] and NAS-UNet but still maintains the characteristics of the encoder and decoder part of the overall network. Figure 4 shows the search space of the upsampling cell. In this search space, the candidate operations for convolution, upsampling, and downsampling are the same as those in the entire-structured search space.

3.4. Two-stage search strategy for PICNNs

Research [1] shows that improper selection of the loss function can have a significant impact on prediction performance. The optimal network architecture searched under an inappropriate loss function cannot effectively improve prediction results. Based on this, this paper adopts a two-stage search strategy, dividing the search process into two stages: 1) loss function search stage and 2) network architecture search stage.

3.4.1. Loss function search stage

All components as well as operations in our search space can be regarded as hyperparameters affecting the loss functions thus hyperparameter optimization can be conducted. For PDEs with different boundary conditions, five sub-networks are randomly searched from the search space as the default network structures. The best loss function is determined based on their average prediction error. For PDEs with different source fields, the original UNet model [27] is used as the default structure. In this paper, the Bayesian optimization based on Gaussian processes [39] and the median stopping strategy [40] are adopted for hyperparameter optimization of the search space. The fundamental principle behind Bayesian optimization is to estimate an unknown function by utilizing a prior distribution and then iteratively select sampling points based on an acquisition function defined by the posterior distribution. The median stopping strategy can be used to terminate their training prematurely. A detailed introduction of these two methods can be seen in Supplementary material C.

3.4.2. Neural network architecture search

After determining the construction of the loss function, we searched for the network architecture. Two neural network architecture search strategies are adopted: multi-trial strategy and one-shot strategy.

For multi-trial strategy, this paper uses policy-based reinforcement learning [41]. The architecture search problem is framed as a reinforcement learning problem, where the task is to train a controller that generates model architectures for PICNNs. The controller is implemented using the LSTM, which progressively generates descriptions of neural network components from the search space. Once the controller generates the entire neural network structure, the reciprocal of the relative L_2 error e on the validation set of the PICNNs will be considered as the reward in reinforcement learning, i.e.:

$$reward = \frac{1}{e} \tag{10}$$

As shown in Figure 5, by using the rewards of the generated PICNN model to update the policy gradient, the policy-based reinforcement learning can learn to optimize the

controller parameters θ so that the controller can find the optimal CNN architecture.

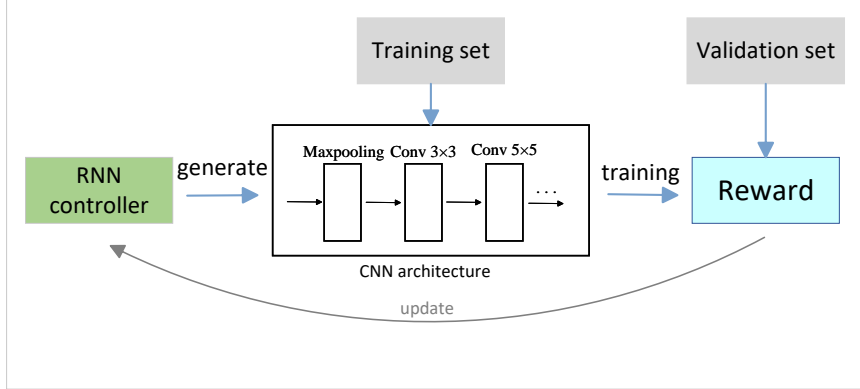


Figure 5: The overview of policy-based reinforcement learning

Specifically, the policy-based reinforcement learning gives the approximation of the policy gradient of θ :

$$\nabla_{\theta} J(\theta) = \sum_{t=1}^T \nabla_{\theta} \log \pi(a_{t+1} | a_t; \theta) \times reward \quad (11)$$

where T is the number of components the controller has to generate, a_t is the component of the neural network generated by the controller from the candidate operations at step t , and $J(\theta)$ represents the expected cumulative rewards. Then, the policy parameters are updated using the stochastic gradient ascent method:

$$\theta \leftarrow \theta + \alpha \nabla_{\theta} J(\theta) \quad (12)$$

where α is the learning rate. The controller continuously generates new CNN architectures until convergence. Finally, the model with the highest reward is selected as the final CNN model.

On the other hand, the one-shot strategy is an efficient method in NAS as it reduces the training time and computational resources during the searching process by training a "supernet" containing all candidate operations of the neural network. Using the one-shot strategy, unlike the multi-trial strategy that requires separate training for each candidate network structure, only one supernet needs to be trained. Once the supernet is trained, the optimal sub-network can be obtained internally. In this paper, we used two one-shot strategy methods: ENAS (Efficient Neural Architecture Search) [42] and DARTS (Differentiable Architecture Search) [38].

Based on policy-based reinforcement learning, ENAS uses weight sharing between child models to accelerate the searching process. Specifically, the controller and child models alternately update weights during the search process.

DARTS is a gradient-based method to search for neural network architectures. It first assigns a learnable weight α to each candidate operation, making the search space continuous and differentiable. The SoftMax function is used over all possible operations to relax the categorical choice of a particular operation, i.e.,

$$o_{i,j}(\mathbf{x}) = \sum_{k=1}^K P_k o_{i,j}^{(k)}(\mathbf{x}) \quad (13)$$

$$P_k = \exp(\alpha_{i,j}^{(k)}) / \sum_{k'=1}^K \exp(\alpha_{i,j}^{(k')}) \quad (14)$$

where $o_{i,j}(\mathbf{x})$ represents the tensor obtained by performing the operation between nodes i and j on input \mathbf{x} , $\alpha_{i,j}^{(k)}$ represents the weight of operation $o_{i,j}^{(k)}$ between nodes i and j , K is the number of candidate operations. DARTS optimizes network weights (i.e., model parameters) and architecture weights (i.e., weights of candidate operations) alternately. This suggests a bilevel optimization problem as follows:

$$\begin{aligned} & \min_{\alpha} L_{\text{val}}(\omega_{\alpha}^*, \alpha) \\ \text{s.t. } & \omega_{\alpha}^* = \operatorname{argmin}_{\omega_{\alpha}} L_{\text{train}}(\omega_{\alpha}, \alpha) \end{aligned} \quad (15)$$

where α is the neural architecture, indicating the relative importance of candidate operations, ω_{α} represents the weights of the architecture. L_{val} is the loss on the validation set, L_{train} is the loss on the training set. At the end of the search, select the operation with the highest weight in all mixed operations to obtain the final architecture.

4. Experiments

The primary objective of the experiments in this section is to **(1)**: Compare the performance of two distinct UNet search spaces, namely cell-based and entire-structured search space within PICNNs. **(2)**: Evaluate two kinds of search strategies used in PICNNs: the multi-trial strategy employing policy-based reinforcement learning, and the one-shot strategy utilizing DARTS and ENAS. These experiments are designed to identify which search space and search strategy yield the most accurate and efficient models for solving PDEs.

4.1. Datasets

The datasets selected for this study cover a broad spectrum of PDEs, including heat equations with different boundary conditions, Poisson equations with varying source fields, Poisson equations with different heat source layouts, Darcy flow with different input property fields, and Navier-Stokes equations with varying geometries. These datasets are publicly available and their adoption in previous studies provides a benchmark for evaluating the performance of our Auto-PICNN framework. Besides, the diversity of the selected datasets ensures our findings are robust and widely applicable across different scenarios in the PICNNs.

Heat equations with different boundary conditions come from the model PhyGeoNet [13], which can be defined as:

$$\begin{cases} \nabla \cdot (\nabla T(x)) = 0, x \in \Omega_p \\ T(x) = T_{bc}(x), x \in \partial \Omega_p \end{cases} \quad (16)$$

where T is the temperature field that we want to solve, Ω_p is the annular-shaped doubly-connected domain, which can be represented as:

$$r < |x - c| < R \quad (17)$$

where c is the center of the annulus, and r and R are the inner and outer radius, respectively. A coordinate transformation on this annulus can yield a regular rectangular region for PICNNs. For the Dirichlet boundary condition T_{bc} , the dataset parameterizes the boundary temperature on the inner circle as the varying constant $T_{in} \in [1, 7]$, while a fixed temperature $T_{out} = 0$ is applied to the outer circle boundary. The model input is the linear interpolation field from the inner boundary T_{in} to the outer boundary T_{out} , which can uniquely represent the varying boundary conditions. $T_{in} = \{1, 7\}$ is used as the training and validation set, while $T_{in} = \{2, 3, 4, 5, 6\}$ is used as the test set.

For the Poisson equation with varying source fields, it comes from PhyGeoNet [13]. Consider a Poisson equation with homogeneous Dirichlet boundary conditions and spatially varying source term $f(x)$ as

$$\begin{cases} \nabla \cdot (\nabla T(x)) + f(x) = 0, x \in \Omega_p \\ T(x) = 10, x \in \partial \Omega_p \end{cases} \quad (18)$$

where the source field $f(x)$ has a dimension of 900 (30×30) on the discrete domain and can be obtained from a Gaussian random field, satisfying:

$$f(x) \sim GP(0, K(x, x_0)) \quad (19)$$

The kernel function has the form:

$$K(x, x_0) = \sigma_0^2 \exp\left(-\frac{(x - x_0)^2}{l^2}\right) \quad (20)$$

The variation of the exponential kernel is controlled by the parameters σ_0 and length scale $l = 0.5$. Due to the smoothness of the field, the Gaussian process can be approximated by the Karhunen-Loève (K-L) expansion:

$$f(x) = \sum_{i=1}^{\infty} \sqrt{\lambda_i} \phi_i(x) \omega_i \quad (21)$$

where λ_i and $\phi_i(x)$ are the eigenvalues and eigenfunctions of the kernel K , respectively; ω_i is an independent random variable with mean 0 and variance 1. This dataset truncates the K-L expansion to the first 10 modes. 256 different source fields are used for the training and validation sets, and 744 different source fields are used for the test set.

Poisson equations with different heat source layouts come from the model PI-UNet [14]. The region of this PDE is a two-dimensional rectangular heat-conducting plate with several rectangle heat source layouts representing electronic components. There is an isothermal region with a length of 0.01m in the middle of the left boundary, which can be considered as the Dirichlet boundary condition. Other boundaries are adiabatic, which can be considered as Neumann boundary conditions with the gradient of the temperature field being 0. This dataset uses 8000 different heat source layouts which are denoted as $f(x)$ in the previously mentioned Poisson equations as input for the training set, 1000 for the validation set, and 1000 for the test set.

Darcy flow with different input property fields comes from the model pde-surrogate [12], which can be defined as:

$$\begin{cases} -\nabla \cdot (K(s) \nabla u(s)) = f(s), s \in S \\ u(s) = u_D(s), s \in \Gamma_D \\ K(s) \nabla u(s) \cdot \mathbf{n} = g(s), s \in \Gamma_N \end{cases} \quad (22)$$

where S is the domain of the PDE, $u(s)$ are the field variables of interest, \mathbf{n} is the unit normal vector of the Neumann boundary Γ_N , and Γ_D is the Dirichlet boundary. The input property field $K(s)$ has a dimension of 64×64 on the discrete domain and can also be obtained from a Gaussian random field. This dataset truncates the K-L expansion to the first 512 modes. The source field $f(s)$ is zero. 4096 different input property fields are used for the training set, 128 for the validation set, and 512 for the test set.

Navier-Stokes equations with varying geometries come from the model PhyGeoNet [13], which can be defined as:

$$\begin{cases} \nabla \cdot \mathbf{v} = 0, \\ (\mathbf{v} \cdot \nabla) \mathbf{v} = \nabla \cdot (\nu \nabla \mathbf{v}) - \nabla p, \end{cases} \quad (23)$$

where \mathbf{v} is the velocity vector, ν is the fluid viscosity, and p is the pressure field. The geometry of the physical domain is described by the coordinates of the left and right vessel walls. These are expressed as functions of a scalar s that varies to represent different degrees of stenosis or aneurysm and the coordinates for the left and right walls are defined by the equations:

$$\begin{cases} x_l = s \cdot \cos(2\pi y) - 0.5, \\ x_r = -s \cdot \cos(2\pi y) + 0.5, \end{cases} \quad (24)$$

The velocity at the inlet is defined as $\mathbf{v} = [0, 0.4]$, and the pressure gradient along the inlet is set to $\nabla p \cdot \mathbf{n} = 0$. No-slip boundary conditions are applied on the curved vessel walls. At the outlet, a traction-free condition is imposed with $\nabla \mathbf{v} \cdot \mathbf{n} = 0$ and $p = 0$, where \mathbf{n} denotes the wall-normal vector. $s = \{-0.1, 0.0, 0.1\}$ is used as the training and validation set, while $s = \{-0.075, -0.05, -0.025, 0.025, 0.05, 0.075\}$ is used as the test set.

4.2. Evaluation metrics

In order to measure the error between the predictions of the PICNNs and the ground truth, we use the relative L_2 error and MAE (Mean Absolute Error) as evaluation metrics. For the heat equations with different boundary conditions, Poisson equations with varying source fields, Darcy flow with different input property fields, and Navier-Stokes equations with varying geometries, the corresponding paper used the relative L_2 error as the evaluation metric, with the expression as follows:

$$L_2 \text{ error} = \frac{\sqrt{\sum_{i=1}^N |u_\theta(x_i) - u(x_i)|^2}}{\sqrt{\sum_{i=1}^N |u(x_i)|^2}} \quad (25)$$

where $u_\theta(x_i)$ and $u(x_i)$ are the prediction of PICNNs and the high-fidelity solution to the PDEs, respectively. For the Poisson equation with different heat source layouts, the corresponding paper used MAE as the evaluation metric. To ensure a fair comparison, we use the same evaluation metrics for analysis and comparison.

Dataset	Search space	Relative L_2 error
Poisson equations with varying source fields	cell-based	0.0229
	entire-structured	0.0135
Poisson equations with different heat source layouts	cell-based	2.21×10^{-4}
	entire-structured	8.34×10^{-5}
Darcy flow with different input property fields	cell-based	0.0323
	entire-structured	0.0065

Table 1: Relative L_2 error on the validation set for the entire-structured and cell-based search space.

Dataset	Search space	Relative L_2 error
Heat equations with different boundary conditions	Reinforcement learning	0.0197
	DARTS	0.0740
	ENAS	0.0602
Poisson equations with varying source fields	Reinforcement learning	0.0120
	DARTS	0.0121
	ENAS	0.0121
Poisson equations with different heat source layouts	Reinforcement learning	5.20×10^{-5}
	DARTS	6.14×10^{-5}
	ENAS	6.89×10^{-5}
Darcy flow with different input property fields	Reinforcement learning	0.0024
	DARTS	0.0041
	ENAS	0.0045
Navier-Stokes equations with varying geometries	Reinforcement learning	0.0747
	DARTS	0.1285
	ENAS	0.1623

Table 2: Relative L_2 error of different search strategies on the validation set

4.3. Comparison between the search space

After conducting a search for 10 different network architectures within the entire-structured and cell-based search space, the smallest relative L_2 error on the validation set among these architectures is selected as the final metric for comparison. The results are shown in Table 1. It can be found that on the validation set, the prediction error of the entire-structured search space is significantly lower than that of the cell-based search space. Therefore, the entire-structured search space of UNet is used as the final search space.

4.4. Comparison between the search strategies

As shown in Table 2, a comparison of the three search strategies was conducted in all five datasets. Among them, we choose the velocity error of the training set as the search objective in Navier-Stokes equations. It is found that the multi-trial search strategy based on policy-based reinforcement learning has significantly lower errors on the validation set compared to DARTS and ENAS (one-shot strategy). Though it takes more time to search, policy-based reinforcement learning is used as the search strategy.

4.5. Implementation details

Each dataset is trained on a single NVIDIA GeForce RTX 4090 GPU. For training, we utilize Adam optimizer with the learning rate of 0.001. We implemented the hyperparameter optimization and neural architecture search with the AutoML toolkit NNI [43]. Due to the difference in training epochs till convergence, the search time varies in different datasets. When searching for the loss function, the heat equations with different boundary conditions take 2 GPU hours, the Poisson equations with varying source fields take 12 GPU hours, the Poisson equations with different heat source layouts take 6 GPU hours, Darcy flow with different input property fields takes 10 GPU hours, and Navier-Stokes equations with varying geometries take 12 GPU hours. When searching for the architecture, the searching time for the above five datasets is 3 GPU hours, 1 GPU day, 1.5 GPU days, 1 GPU day and 1 GPU day respectively. The training epochs for the above datasets are 1000, 10000, 30, 300 and 20000 respectively with batch size being 1 for Poisson equations with different heat source layouts and 32 for Poisson equations with varying source fields and Darcy flow. The number of batches for heat equations with different boundary conditions and Navier-Stokes equations is one. The number of channels for the standard CNN is [16,32,32,16] and the initial channel for the UNet is 32.

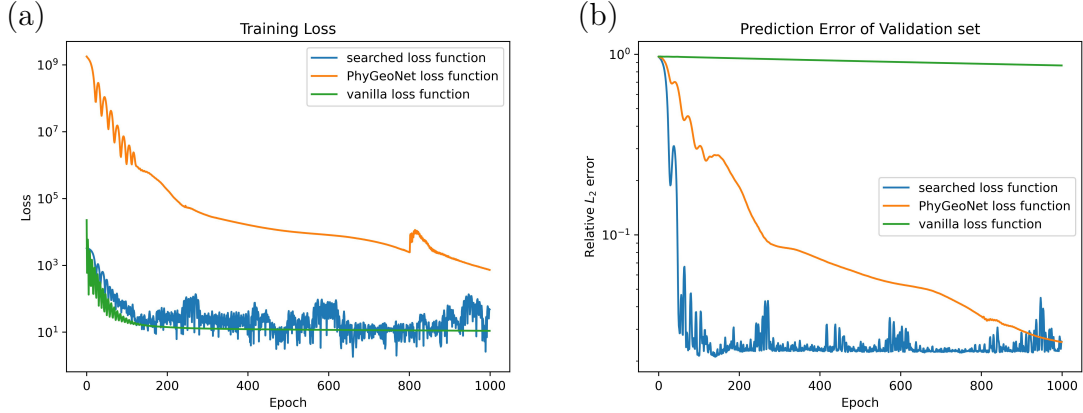


Figure 6: Heat equation with different boundary conditions: PDE-driven loss and prediction error using the loss function after searching, the loss function of baseline model and the vanilla MSE loss function. (a) shows the training loss under these loss functions while (b) shows the relative L_2 error on the validation sets.

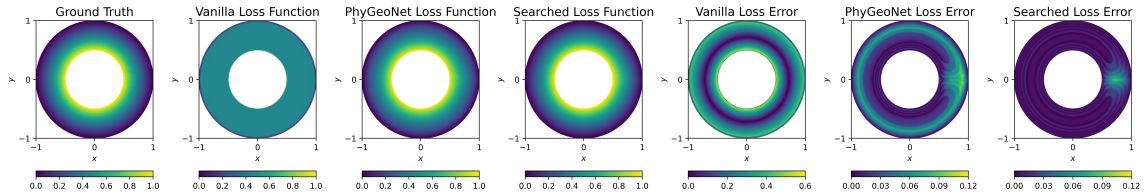


Figure 7: Heat equation with different boundary conditions: The ground truth, the predicted solutions and the point-wise prediction error using different loss functions

5. Results

5.1. Loss function

In this paper, the PICNNs (PhyGeoNet[13], PI-UNet[14], PDE-surrogate[12]) corresponding to the above-mentioned five datasets were selected as the baseline models. We first compare the loss function after searching with the vanilla loss function and those of the baseline models.

For heat equations with different boundary conditions, PhyGeoNet [13] is chosen as the baseline model for this dataset. Figure 6 shows the training curve of PDE-driven loss and relative prediction error using the loss function after searching, the loss function of the baseline model and the vanilla MSE loss function. The results show the loss function after searching significantly reduces the relative L_2 error on

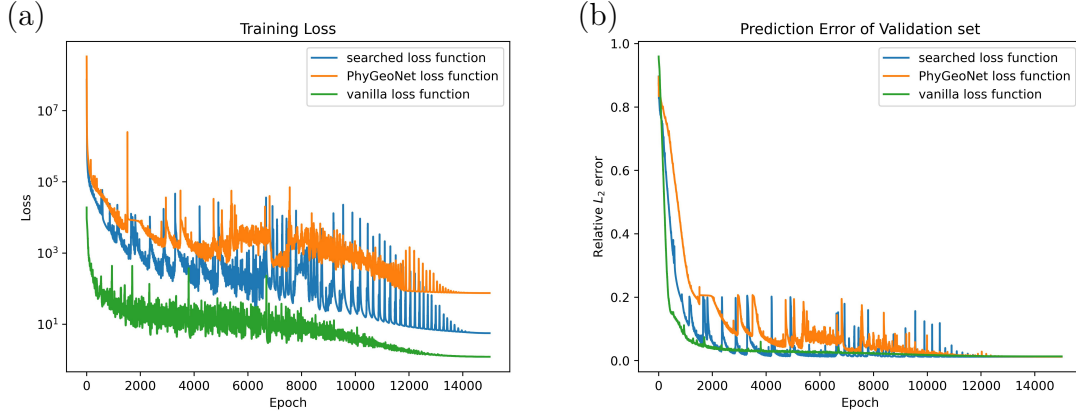


Figure 8: Poisson equations with varying source fields: PDE-driven loss and prediction error using the loss function after searching, the loss function of baseline model and the vanilla MSE loss function. (a) shows the training loss under these loss functions while (b) shows the relative L_2 error on the validation sets.

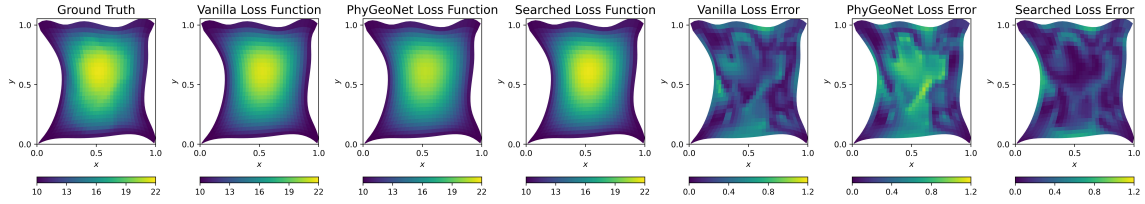


Figure 9: Poisson equations with varying source fields: The ground truth, the predicted solutions and the point-wise prediction error using different loss functions

the validation set. This can also be illustrated by showing the predicted solutions derived from various loss functions and visualising their point-wise errors against the ground truth. (see Figure 7). Since there are multiple samples in the validation set, we randomly choose one to show the visualization result. From the second subfigure of Figure 7, we can see that although the vanilla loss function can converge, it may fall into a trivial solution due to its use of a soft constraint, preventing the model from correctly solving this PDE. In contrast, the hard constraint, which is both the searched result and is used in the baseline model, can approximate the true solution. This demonstrates the importance of the hard constraint in solving certain PDEs.

For poisson equations with varying source fields, PhyGeoNet [13] is chosen as the baseline model. Figure 8 shows the training curve of PDE-driven loss and relative prediction error. We can see that the relative L_2 error of the searched-based loss

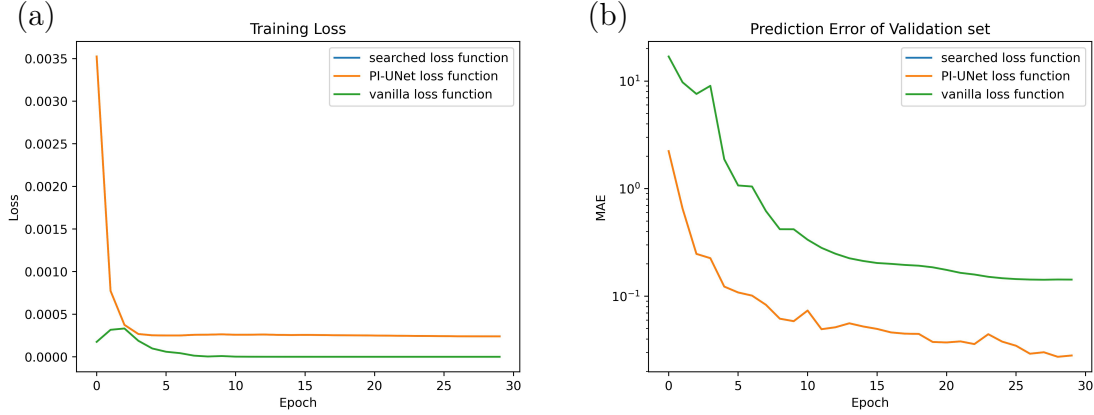


Figure 10: Poisson equations with different heat source layouts: PDE-driven loss and prediction error using the loss function after searching, the loss function of baseline model and the vanilla MSE loss function. (a) shows the training loss under these loss functions while (b) shows the mean absolute error on the validation sets. The blue line and the orange line overlap.

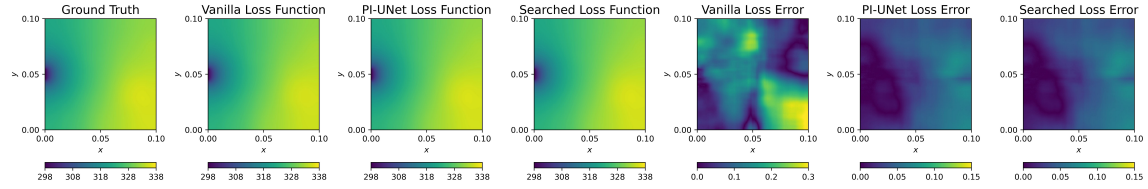


Figure 11: Poisson equations with varying source fields: The ground truth, the predicted solutions and the point-wise prediction error using different loss functions

function is slightly better than the vanilla loss function. Figure 9 also shows the visualization result of the predicted solutions and point-wise error of a randomly selected sample in the validation sets.

For poisson equations with different heat source layouts, PI-UNet [14] is chosen as the baseline model. Figure 10 shows the training curve of PDE-driven loss and relative prediction error. In this dataset, the searched-based loss function is the same as the baseline model. Figure 11 shows the visualization result of the predicted solutions and point-wise error.

For darcy flow with different input property fields, PDE-surrogate [12] is chosen as the baseline model. Figure 12 shows the training curve of PDE-driven loss and relative prediction error. In this dataset, we can observe the training loss of the search-based loss function is higher than the loss function in the baseline model and

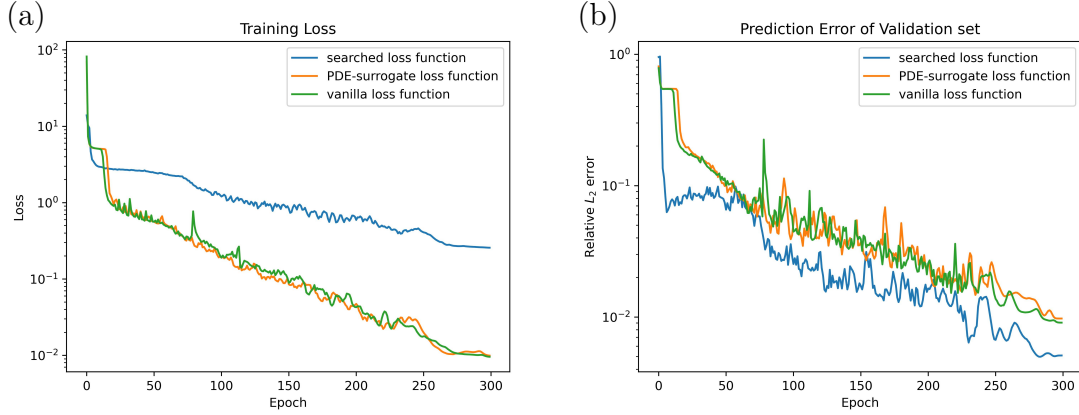


Figure 12: Darcy flow with different input property fields: PDE-driven loss and prediction error using the loss function after searching, the loss function of baseline model and the vanilla MSE loss function. (a) shows the training loss under these loss functions while (b) shows the relative L_2 error on the validation sets.

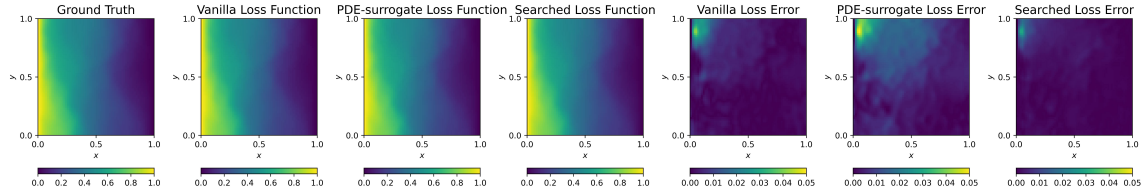


Figure 13: Darcy flow with different input property fields: The ground truth, the predicted solutions and the point-wise prediction error using different loss functions

the vanilla loss function but the relative L_2 error is lower than those. Apart from the trivial solution that appeared in heat equations with different boundary conditions, different kernels for numerical calculations as well as different operators will all lead to differences in the value of loss function. This further validates our above-mentioned finding that the PDE-driven loss and relative prediction error are not uniform. The visualization result of the predicted solutions and point-wise error shown in Figure 13 also demonstrate our search-based loss function performs better in solving PDEs especially in areas with significant changes.

For Navier-Stokes equations with varying geometries, PhyGeoNet [13] is chosen as the baseline model. Figure 14 shows the training curve of PDE-driven loss and relative prediction error about the pressure. We can still observe the inconsistency between the training loss and the relative L_2 error. Figure 15 shows the visualization

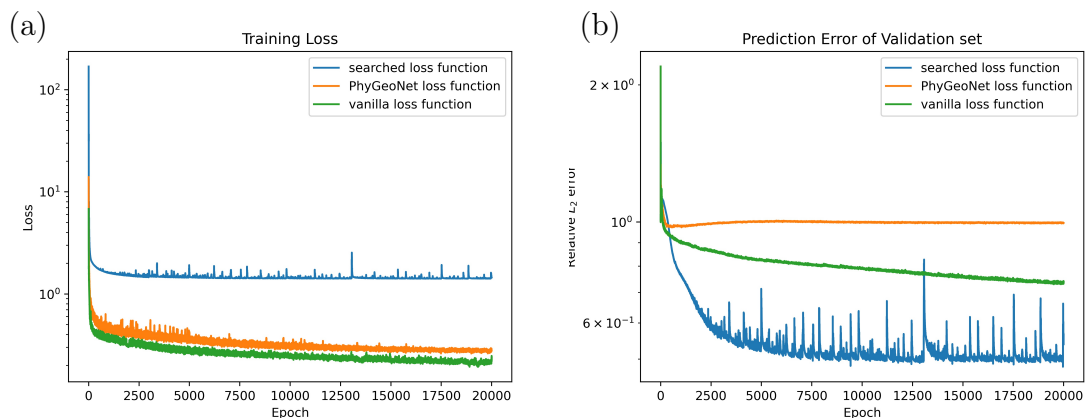


Figure 14: Navier-Stokes equations with varying geometries: PDE-driven loss and prediction error using the loss function after searching, the loss function of baseline model and the vanilla MSE loss function. (a) shows the training loss under these loss functions while (b) shows the relative L_2 error on the validation sets.

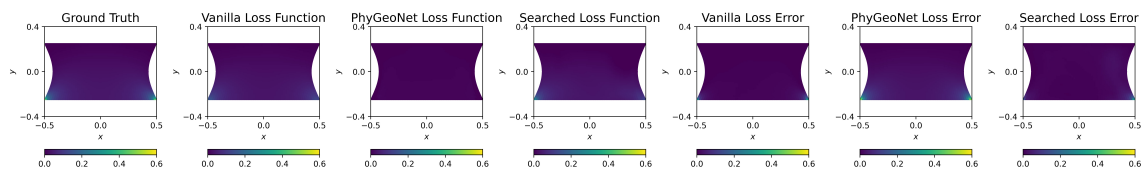


Figure 15: Navier-Stokes equations with varying geometries: The ground truth, the predicted solutions and the point-wise prediction error using different loss functions

result of the predicted solutions and point-wise error about the pressure.

Table 3 displays the specific values of the prediction errors in solving PDEs on all five datasets under different loss functions. The results demonstrate the superiority of our loss function searching framework. The search results for the components and operations of the loss function can be seen in Supplementary Table 1 which also highlights that different PDE datasets exhibit a preference for different loss functions.

5.2. Comparison with the baseline models

The baseline models corresponding to the five datasets were compared with the models obtained through our automated machine learning methods (including the search for loss function and network architecture). For each dataset, both the baseline model and the search-based model were trained and tested on the same set.

Dataset	Loss function	Error	
Heat equations with different boundary conditions	Vanilla MSE loss	0.7421	
	Baseline model	0.0478	
	searched	0.0242	
Poisson equations with varying source fields	Vanilla MSE loss	0.0133	
	Baseline model	0.0123	
	searched	0.0121	
Poisson equations with different heat source layouts	Vanilla MSE loss	0.1428	
	Baseline model	0.0227	
	searched	0.0227	
Darcy flow with different input property fields	Vanilla MSE loss	0.0094	
	Baseline model	0.0090	
	searched	0.0042	
Navier-Stokes equations with varying geometries	Vanilla MSE loss	0.0899	0.5242
	Baseline model	0.0939	0.4057
	searched	0.0747	0.4057

Table 3: Error (mean absolute error for the Poisson equations with different source layouts and relative L_2 error for the other datasets) when using the vanilla loss function (MSE), baseline models' loss function and the search-based loss function. For Navier-Stokes equations with varying geometries, the first column of the error is the velocity error while the second column is the pressure error

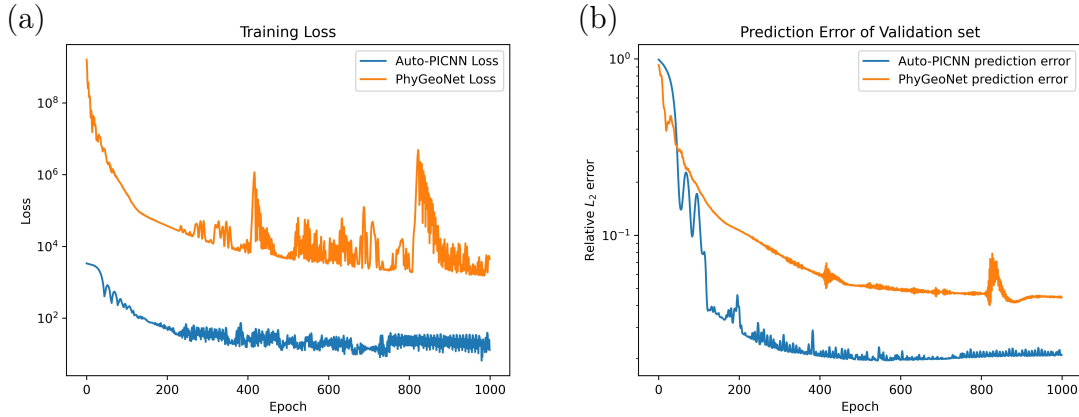


Figure 16: Heat equation with different boundary conditions: PDE-driven loss and prediction error of Auto-PICNN and the baseline model PhyGeoNet. (a) shows the training loss while (b) shows the relative L_2 error on the test sets.

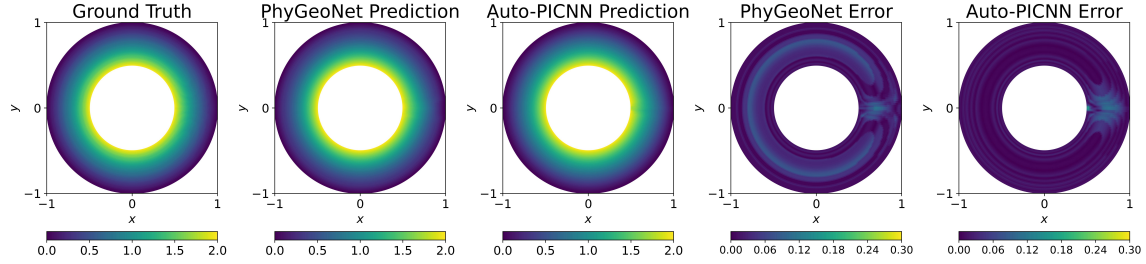


Figure 17: Heat equation with different boundary conditions: The ground truth, the predicted solutions of the baseline model, the predicted solutions of Auto-PICNN, the point-wise prediction error of the baseline model, and the point-wise prediction error of Auto-PICNN

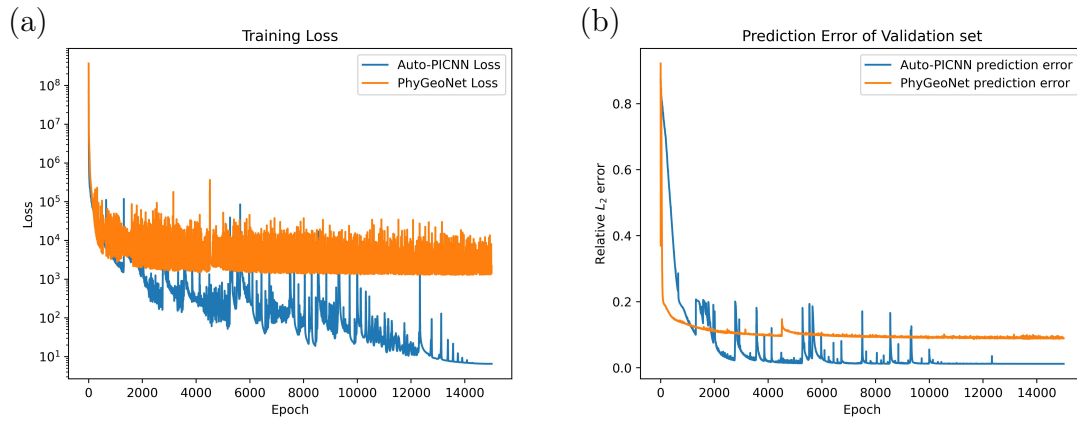


Figure 18: Poisson equations with varying source fields: PDE-driven loss and prediction error of Auto-PICNN and the baseline model PhyGeoNet. (a) shows the training loss while (b) shows the relative L_2 error on the test sets

For heat equations with different boundary conditions, Figure 16 shows the training curve of PDE-driven loss and relative prediction error of the baseline model PhyGeoNet and Auto-PICNN. Figure 17 shows the predicted solution and point-wise error against the ground truth of the baseline model and Auto-PICNN.

For poisson equations with varying source fields, Figure 18 shows the training curve of PDE-driven loss and relative prediction error of the baseline model PhyGeoNet and Auto-PICNN. Figure 19 shows the predicted solution and point-wise error against the ground truth of the baseline model and Auto-PICNN.

For poisson equations with different heat source layouts, Figure 20 shows the

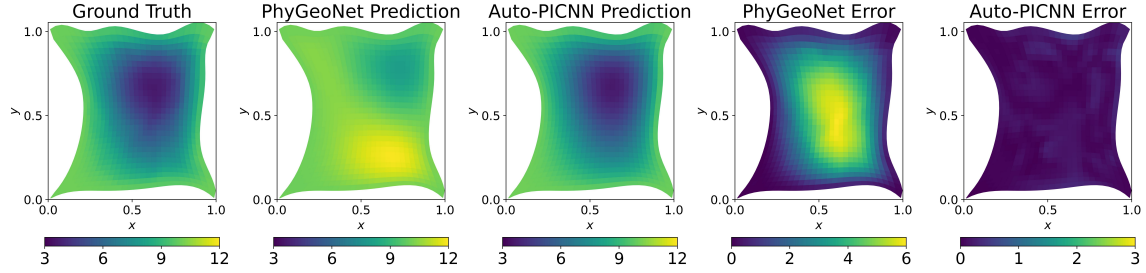


Figure 19: Poisson equations with varying source fields: TThe ground truth, the predicted solutions of the baseline model, the predicted solutions of Auto-PICNN, the point-wise prediction error of the baseline model, and the point-wise prediction error of Auto-PICNN

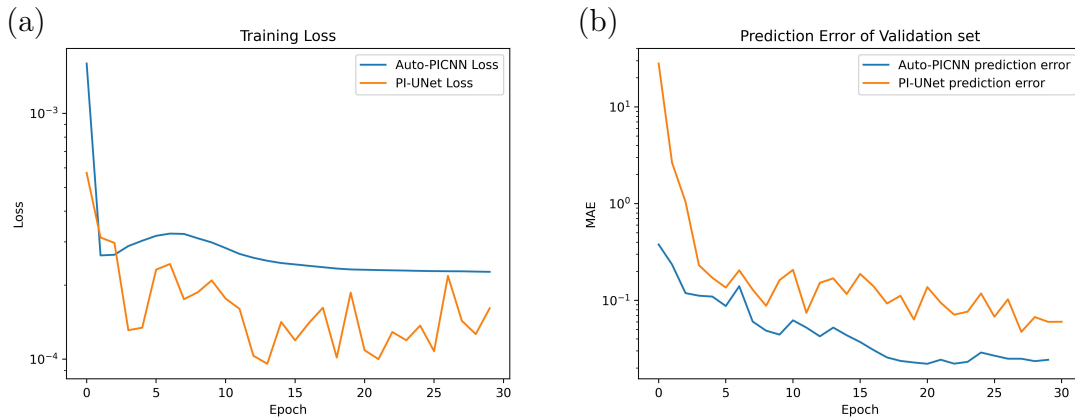


Figure 20: Poisson equations with different heat source layouts: PDE-driven loss and prediction error of Auto-PICNN and the baseline model PI-UNet. (a) shows the training loss while (b) shows the mean absolute error on the test sets

training curve of PDE-driven loss and relative prediction error of the baseline model PI-UNet and Auto-PICNN. Figure 21 shows the predicted solution and point-wise error against the ground truth of the baseline model and Auto-PICNN.

For darcy flow with different input property fields, Figure 22 shows the training curve of PDE-driven loss and relative prediction error of the baseline model PDE-surrogate and Auto-PICNN. Figure 23 shows the predicted solution and point-wise error against the ground truth of the baseline model and Auto-PICNN.

For Navier-Stokes equations with varying geometries, Figure 24 shows the training curve of PDE-driven loss and relative prediction error of the pressure of the baseline model PhyGeoNet and Auto-PICNN. Figure 25 shows the predicted solution of the

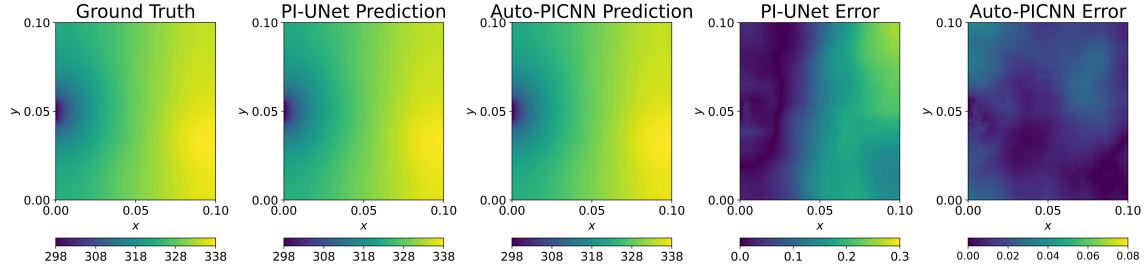


Figure 21: Poisson equations with varying source fields: The ground truth, the predicted solutions of the baseline model, the predicted solutions of Auto-PICNN, the point-wise prediction error of the baseline model, and the point-wise prediction error of Auto-PICNN

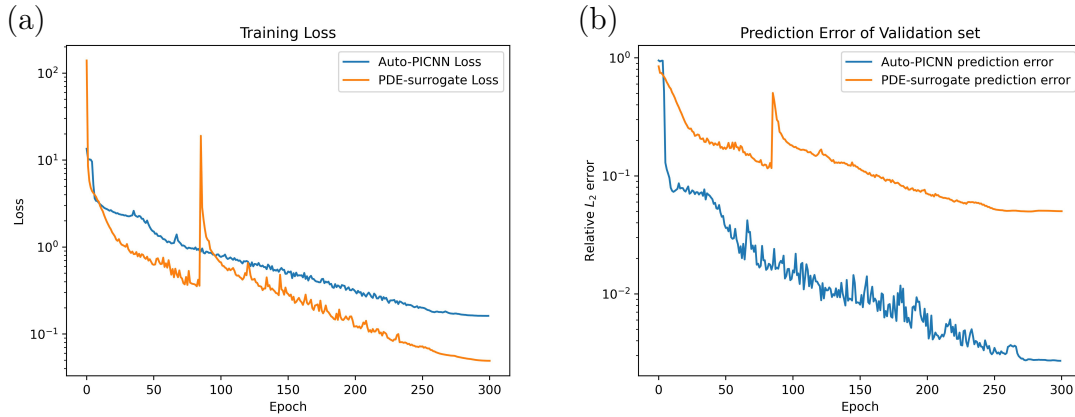


Figure 22: Darcy flow with different input property fields: PDE-driven loss and prediction error of Auto-PICNN and the baseline model PDE-surrogate. (a) shows the training loss while (b) shows the relative L_2 error on the test sets

pressure and point-wise error against the ground truth of the baseline model and Auto-PICNN.

The above figures show that our automated learning method used in this paper significantly reduced the prediction error compared to the baseline models when solving PDEs. The numerical results are shown in Tables 4 and 5. The superiority of Auto-PICNN ensures that it can be applied to solve a wide range of PDEs with different characteristics.

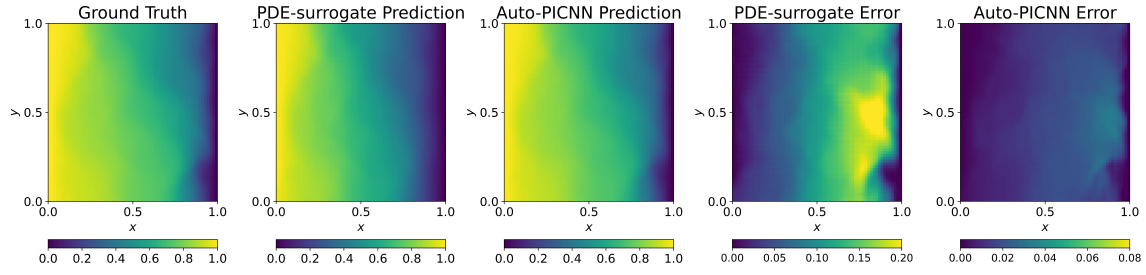


Figure 23: Darcy flow with different input property fields: The ground truth, the predicted solutions and the point-wise prediction error of baseline model and Auto-PICNN

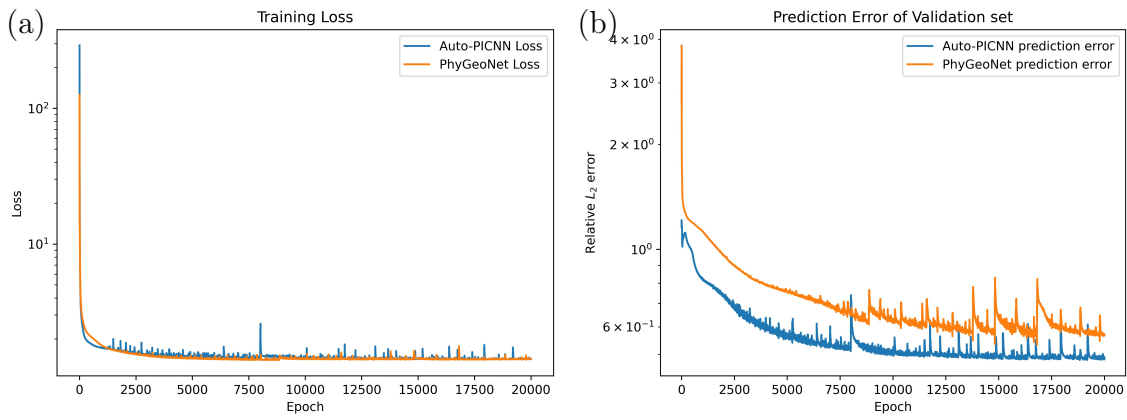


Figure 24: Navier-Stokes equations with varying geometries: PDE-driven loss and prediction error of Auto-PICNN and the baseline model PhyGeoNet. (a) shows the training loss while (b) shows the relative L_2 error on the test sets

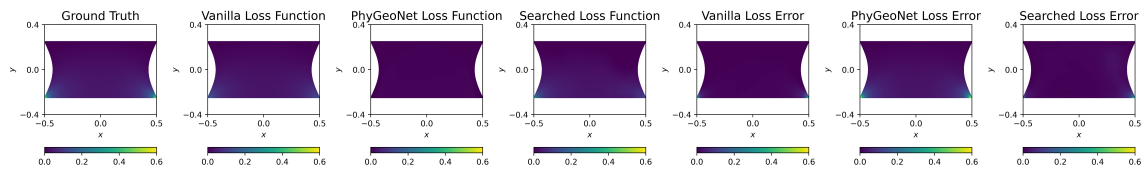


Figure 25: Navier-Stokes equations with varying geometries: The ground truth, the predicted solutions of the baseline model, the predicted solutions of Auto-PICNN, the point-wise prediction error of the baseline model, and the point-wise prediction error of Auto-PICNN

Dataset	Model	MAE
Poisson equations with different heat source layouts	PI-UNet	0.0271
	Auto-PICNN	0.0162

Table 4: MAE on the test set for the baseline model PI-UNet and the model obtained through automated machine learning

Dataset	Model	L_2 Error	
Heat equations with different boundary conditions	PhyGeoNet	0.0523	
	Auto-PICNN	0.0192	
Poisson equations with varying source fields	PhyGeoNet	0.0744	
	Auto-PICNNL	0.0131	
Darcy flow with different input property fields	PDE-surrogate	0.028	
	Auto-PICNN	0.0032	
Navier-Stokes equations with varying geometries	PhyGeoNets	0.0797	0.3543
	Auto-PICNN	0.0564	0.2966

Table 5: Relative L_2 errors on the test set for the baseline model and the model obtained through automated machine learning. For Navier-Stokes equations with varying geometries, the first column of the error is the velocity error while the second column is the pressure error

6. Conclusion

Aiming to find PICNNs adapted to different PDEs and lower their prediction error, this paper uses AutoML to search for loss functions and network architectures. Firstly, we choose the prediction error on the validation set as the search objective. Then we establish novel search spaces for loss function and network architecture including search spaces based on standard CNN architecture and entire-structured search spaces based on UNet. Finally, a two-stage search strategy was adopted. In the loss function search stage, the Bayesian optimization method and the median stopping strategy are used. In the network architecture search stage, policy-based reinforcement learning is selected as the final search strategy. Experiments show that our AutoML method significantly reduces the prediction error compared to the baseline models when solving PDEs, providing new ideas and methods for the development of the PICNNs and PINNs.

However, decoupling the search of loss functions and network architectures may lead to a locally optimal solution. Nowadays, in the field of AutoML, there are only a few studies dedicated to combining neural architecture search and hyperparameter optimization. In future work, the loss function and network architecture of PICNNs may be jointly searched to obtain a globally optimal solution.

Codes availability

The codes and datasets for Auto-PICNN can be downloaded from ¹.

Author contribution statement

Wanyun Zhou: Conceptualization, Data curation, Investigation, Methodology, Software, Writing – original draft

Xiaowen Chu: Conceptualization, Funding acquisition, Project administration, Resources, Supervision, Writing – review and editing

References

- [1] L. Lu, X. Meng, Z. Mao, G. E. Karniadakis, Deepxde: A deep learning library for solving differential equations, *SIAM review* 63 (1) (2021) 208–228.
- [2] J. Sirignano, K. Spiliopoulos, Dgm: A deep learning algorithm for solving partial differential equations, *Journal of computational physics* 375 (2018) 1339–1364.
- [3] S. Markidis, The old and the new: Can physics-informed deep-learning replace traditional linear solvers?, *Frontiers in big Data* 4 (2021) 669097.
- [4] S. Cuomo, V. S. Di Cola, F. Giampaolo, G. Rozza, M. Raissi, F. Piccialli, Scientific machine learning through physics-informed neural networks: Where we are and what’s next, *Journal of Scientific Computing* 92 (3) (2022) 88.
- [5] M. Raissi, P. Perdikaris, G. E. Karniadakis, Physics-informed neural networks: A deep learning framework for solving forward and inverse problems involving nonlinear partial differential equations, *Journal of Computational physics* 378 (2019) 686–707.
- [6] L. Lu, P. Jin, G. E. Karniadakis, Deeponet: Learning nonlinear operators for identifying differential equations based on the universal approximation theorem of operators, *arXiv preprint arXiv:1910.03193* (2019).
- [7] Z. Li, N. Kovachki, K. Azizzadenesheli, B. Liu, K. Bhattacharya, A. Stuart, A. Anandkumar, Fourier neural operator for parametric partial differential equations, *arXiv preprint arXiv:2010.08895* (2020).

¹<https://github.com/wanyunzh/AutoML-for-PICNN>

- [8] S. Huang, W. Feng, C. Tang, J. Lv, Partial differential equations meet deep neural networks: A survey, arXiv preprint arXiv:2211.05567 (2022).
- [9] P.-H. Chiu, J. C. Wong, C. Ooi, M. H. Dao, Y.-S. Ong, Can-pinn: A fast physics-informed neural network based on coupled-automatic-numerical differentiation method, *Computer Methods in Applied Mechanics and Engineering* 395 (2022) 114909.
- [10] G. E. Karniadakis, I. G. Kevrekidis, L. Lu, P. Perdikaris, S. Wang, L. Yang, Physics-informed machine learning, *Nature Reviews Physics* 3 (6) (2021) 422–440.
- [11] Z. Wenshu, L. Daolun, S. Luhang, Z. Wen, L. Xuliang, Review of neural network-based methods for solving partial differential equations, *Chinese Journal of Theoretical and Applied Mechanics* 54 (3) (2022) 543–556.
- [12] Y. Zhu, N. Zabaras, P.-S. Koutsourelakis, P. Perdikaris, Physics-constrained deep learning for high-dimensional surrogate modeling and uncertainty quantification without labeled data, *Journal of Computational Physics* 394 (2019) 56–81.
- [13] H. Gao, L. Sun, J.-X. Wang, Phygeonet: Physics-informed geometry-adaptive convolutional neural networks for solving parameterized steady-state pdes on irregular domain, *Journal of Computational Physics* 428 (2021) 110079.
- [14] X. Zhao, Z. Gong, Y. Zhang, W. Yao, X. Chen, Physics-informed convolutional neural networks for temperature field prediction of heat source layout without labeled data, *Engineering Applications of Artificial Intelligence* 117 (2023) 105516.
- [15] S. Zhang, C. Zhang, B. Wang, Mrf-pinn: A multi-receptive-field convolutional physics-informed neural network for solving partial differential equations, arXiv preprint arXiv:2209.03151 (2022).
- [16] A. T. Mohan, N. Lubbers, D. Livescu, M. Chertkov, Embedding hard physical constraints in neural network coarse-graining of 3d turbulence, arXiv preprint arXiv:2002.00021 (2020).
- [17] P. Ren, C. Rao, Y. Liu, J.-X. Wang, H. Sun, Phycrnet: Physics-informed convolutional-recurrent network for solving spatiotemporal pdes, *Computer Methods in Applied Mechanics and Engineering* 389 (2022) 114399.
- [18] N. Geneva, N. Zabaras, Modeling the dynamics of pde systems with physics-constrained deep auto-regressive networks, *Journal of Computational Physics* 403 (2020) 109056.

- [19] Z. Zhang, X. Yan, P. Liu, K. Zhang, R. Han, S. Wang, A physics-informed convolutional neural network for the simulation and prediction of two-phase darcy flows in heterogeneous porous media, *Journal of Computational Physics* 477 (2023) 111919.
- [20] R. Zhang, Y. Liu, H. Sun, Physics-guided convolutional neural network (phycnn) for data-driven seismic response modeling, *Engineering Structures* 215 (2020) 110704.
- [21] X. Wu, D. Zhang, M. Zhang, C. Guo, S. Zhao, Y. Zhang, H. Wang, B. Yang, Autopinn: When automl meets physics-informed neural networks, *arXiv preprint arXiv:2212.04058* (2022).
- [22] E. Skomski, J. Drgoňa, A. Tuor, Automating discovery of physics-informed neural state space models via learning and evolution, in: *Learning for Dynamics and Control*, PMLR, 2021, pp. 980–991.
- [23] Y. Wang, X. Han, C.-Y. Chang, D. Zha, U. Braga-Neto, X. Hu, Auto-pinn: understanding and optimizing physics-informed neural architecture, *arXiv preprint arXiv:2205.13748* (2022).
- [24] J. Yu, L. Lu, X. Meng, G. E. Karniadakis, Gradient-enhanced physics-informed neural networks for forward and inverse pde problems, *Computer Methods in Applied Mechanics and Engineering* 393 (2022) 114823.
- [25] L. McClenny, U. Braga-Neto, Self-adaptive physics-informed neural networks using a soft attention mechanism, *arXiv preprint arXiv:2009.04544* (2020).
- [26] H. Guo, X. Zhuang, T. Rabczuk, Stochastic analysis of heterogeneous porous material with modified neural architecture search (nas) based physics-informed neural networks using transfer learning, *arXiv preprint arXiv:2010.12344* (2020).
- [27] O. Ronneberger, P. Fischer, T. Brox, U-net: Convolutional networks for biomedical image segmentation, in: *Medical Image Computing and Computer-Assisted Intervention–MICCAI 2015: 18th International Conference, Munich, Germany, October 5-9, 2015, Proceedings, Part III* 18, Springer, 2015, pp. 234–241.
- [28] G. Huang, Z. Liu, L. Van Der Maaten, K. Q. Weinberger, Densely connected convolutional networks, in: *Proceedings of the IEEE conference on computer vision and pattern recognition*, 2017, pp. 4700–4708.

- [29] V. Badrinarayanan, A. Kendall, R. Cipolla, Segnet: A deep convolutional encoder-decoder architecture for image segmentation, *IEEE transactions on pattern analysis and machine intelligence* 39 (12) (2017) 2481–2495.
- [30] A. Mavi, A. C. Bekar, E. Haghighat, E. Madenci, An unsupervised latent/output physics-informed convolutional-lstm network for solving partial differential equations using peridynamic differential operator, *Computer Methods in Applied Mechanics and Engineering* 407 (2023) 115944.
- [31] Y. Wang, L. Zhong, Nas-pinn: neural architecture search-guided physics-informed neural network for solving pdes, *Journal of Computational Physics* 496 (2024) 112603.
- [32] Y. Xie, Y. Ma, Y. Wang, Automatic boundary fitting framework of boundary dependent physics-informed neural network solving partial differential equation with complex boundary conditions, *Computer Methods in Applied Mechanics and Engineering* 414 (2023) 116139.
- [33] C. Wang, S. Li, D. He, L. Wang, Is l^2 physics informed loss always suitable for training physics informed neural network?, *Advances in Neural Information Processing Systems* 35 (2022) 8278–8290.
- [34] J. Long, E. Shelhamer, T. Darrell, Fully convolutional networks for semantic segmentation, in: *Proceedings of the IEEE Conference on Computer Vision and Pattern Recognition (CVPR)*, 2015.
- [35] L.-C. Chen, G. Papandreou, I. Kokkinos, K. Murphy, A. L. Yuille, Deeplab: Semantic image segmentation with deep convolutional nets, atrous convolution, and fully connected crfs, *IEEE Transactions on Pattern Analysis and Machine Intelligence* 40 (4) (2018) 834–848. doi:10.1109/TPAMI.2017.2699184.
- [36] X. He, K. Zhao, X. Chu, Automl: A survey of the state-of-the-art, *Knowledge-Based Systems* 212 (2021) 106622.
- [37] Y. Weng, T. Zhou, Y. Li, X. Qiu, Nas-unet: Neural architecture search for medical image segmentation, *IEEE access* 7 (2019) 44247–44257.
- [38] H. Liu, K. Simonyan, Y. Yang, Darts: Differentiable architecture search, *arXiv preprint arXiv:1806.09055* (2018).
- [39] J. Bergstra, R. Bardenet, Y. Bengio, B. Kégl, Algorithms for hyper-parameter optimization, *Advances in neural information processing systems* 24 (2011).

- [40] D. Golovin, B. Solnik, S. Moitra, G. Kochanski, J. Karro, D. Sculley, Google vizier: A service for black-box optimization, in: Proceedings of the 23rd ACM SIGKDD international conference on knowledge discovery and data mining, 2017, pp. 1487–1495.
- [41] B. Zoph, Q. V. Le, Neural architecture search with reinforcement learning, arXiv preprint arXiv:1611.01578 (2016).
- [42] H. Pham, M. Guan, B. Zoph, Q. Le, J. Dean, Efficient neural architecture search via parameters sharing, in: International conference on machine learning, PMLR, 2018, pp. 4095–4104.
- [43] Microsoft, Neural Network Intelligence (1 2021).
URL <https://github.com/microsoft/nni>